Inventory of Supplemental Information:

- **Supplemental Data,** Behavioral data
- **Figure S1,** relates to Figure 1 & 4
- **Figure S2,** relates to Figure 1
- **Figure S3,** relates to Figure 2
- **Figure S4,** relates to Figure 4
- **Figure S5,** relates to Figure 4
- **Figure S6,** relates to Figure 3 & 4
- **Figure S7,** relates to Figure 5 & 6
- **Figure S8,** relates to Figure 5 & 6
- **Table S1,** relates to Figure 1
- **Supplemental Experimental Procedures**
- **Supplemental References**

Supplemental Data

Behavioral data

Behavioral data showed that subjects performed well on the task, matching previously publish data (Foster et al., 2012). As shown in Figure S2, mean reaction time (RT) was consistent across conditions, excluding the math condition, where mean RT was longer in duration as previously reported (RT mean/standard error: self-episodic = 2.73/0.20; self-semantic = 2.68/0.19; self-judgment = 2.51/0.19; self-other = 2.77/0.29 & math = 4.17/0.54 seconds). Behaviorally, the ratio of true and false responses, respectively, for each condition was as follows: self-episodic (70/30%), self-semantic (48/52%), self-judgment (70/30%), self-other (66/34%) and math (56/44%), matching the equal task occurrence of true and false math equations (mean subject accuracy 88.3% correct). Non-parametric resampling statistics (1000 samples) showed no significant difference in the mean RT between true and false responses across conditions (self-episodic $p = 0.18$; self-semantic $p = 0.47$; self-judgment $p = 0.62$; self-other $p = 0.9$; math $p = 0.94$).

Supplemental Figures

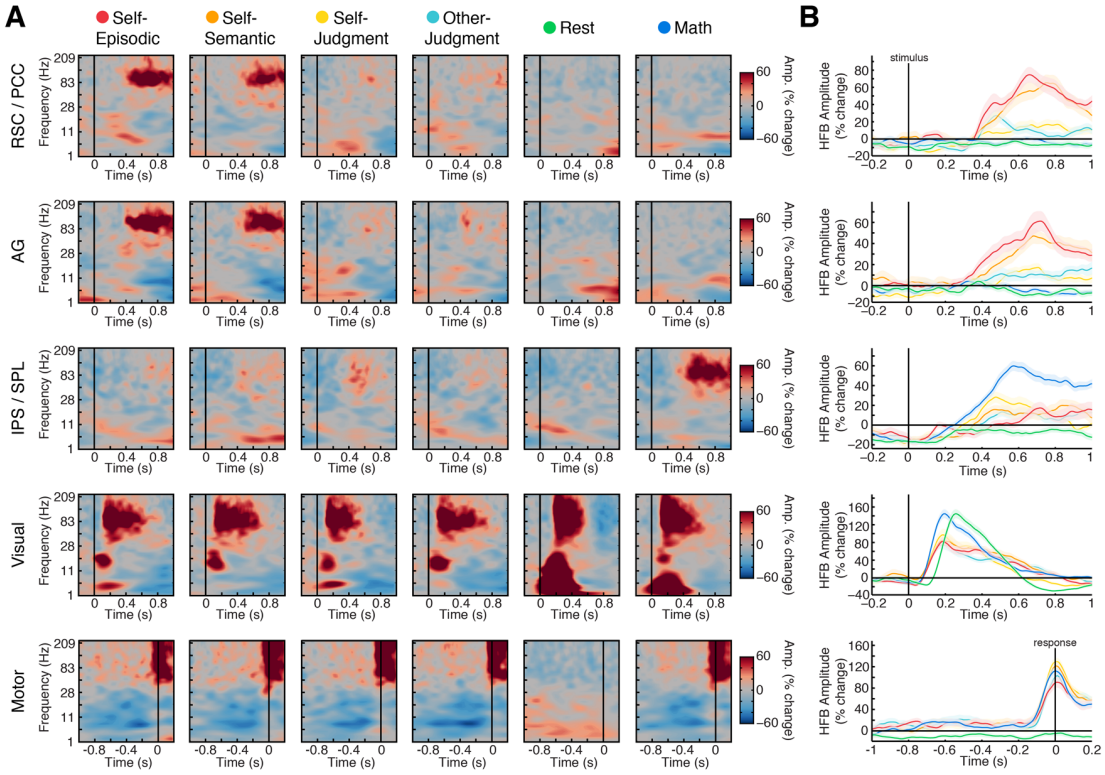

Figure S1 [Related to Figures 1 and 4]. Time-frequency maps and HFB time course
A) Time-frequency plots are show for example electrodes from RSC/PCC, AG, IPS/SPL, Visual and Motor regions (rows). Time-frequency plots display the mean percent change in amplitude for stimulus locked (RSC/PCC, AG, IPS/SPL, Visual) and response locked (Motor) data for each task condition (columns). B) HFB (70-180 Hz) time series plots are shown for the same example locations as in (A). Trace plots display the mean percent change in HFB activity (with standard error of mean) for each task condition. Time-frequency and HFB time course plots highlight differential response timing and selectivity to task conditions across regions. Time-frequency plots also support the focus on HFB activity as the key spectral marker of cortical response.

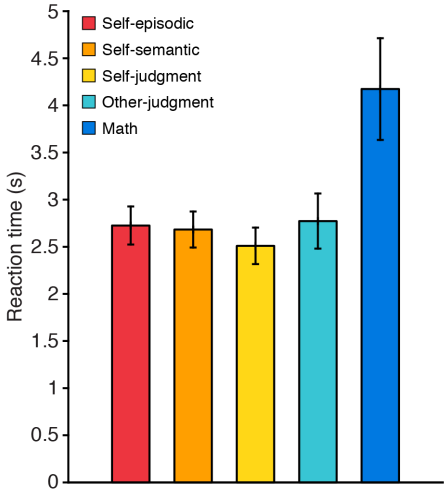

Figure S2 [Related to Figure 1]. Task reaction times
Mean reaction times (with standard error of mean) across task conditions for all subjects.

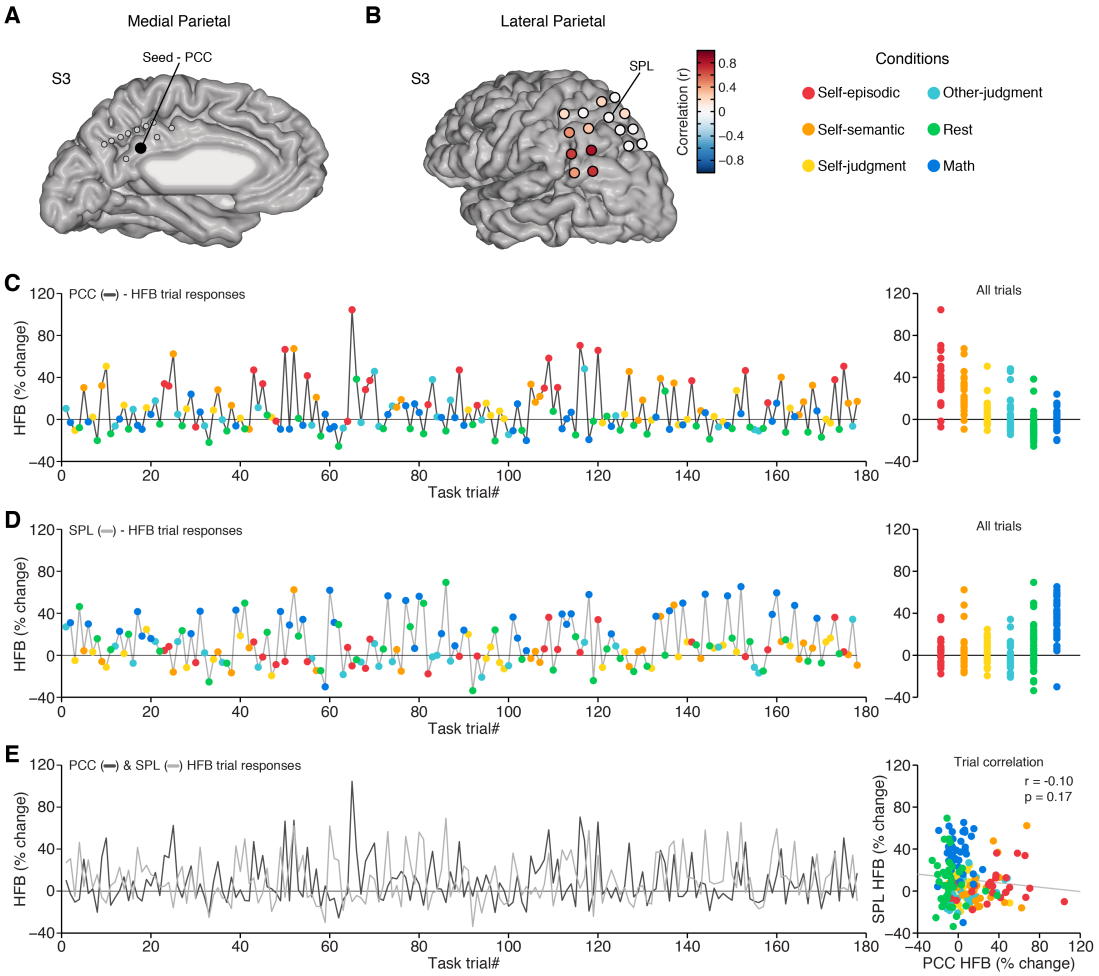

Figure S3 [Related to Figure 2]. Lack of correlation between PCC and SPL during task
A) Medial view of electrode sites for S3, with a PCC seed electrode highlighted. B) Lateral view of electrode sites in S3, where color indicates the correlation value of task responses with respect to the PCC seed electrode in (A). C) HFB responses for all trials (n = 178) across a single experimental run for the PCC electrode in (A). D) Single trial HFB responses for the SPL electrode in (B) from the same experimental data as in (C). E) Time series of trial responses from (C) and (D) reflecting PCC and SPL respectively, display no significant correlation. Scatter plot displays all trial responses for PCC versus SPL.

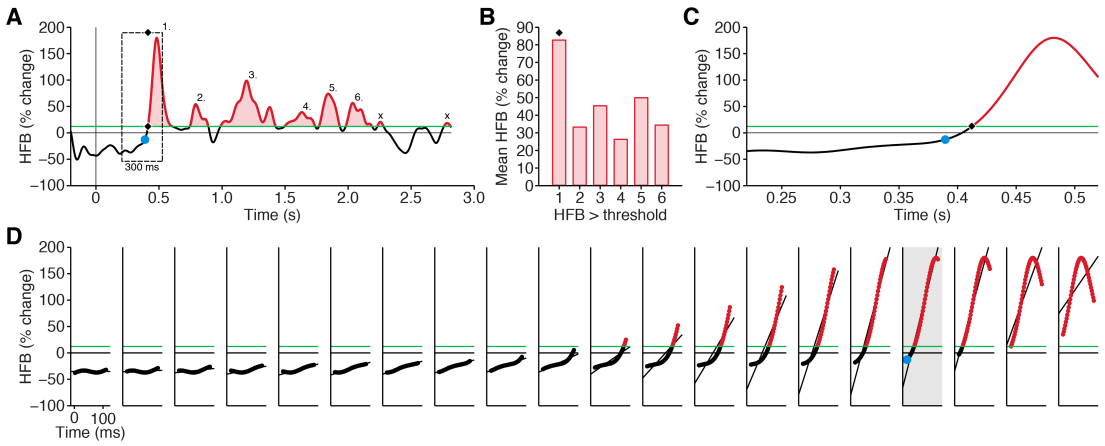

Figure S4 [Related to Figure 4]. Estimation of HFB response onset latency (ROL)
Estimation of HFB ROL was performed at the single trial level. A) For a given trial the entire HFB amplitude epoch is extracted, including the inter-stimulus interval (200 ms). Contiguous time points of supra-threshold HFB amplitude (red trace color) are identified (minimum of 100 ms duration, threshold defined by 2 standard deviations of permuted data, green line). B) When multiple (non-contiguous) supra threshold events are detected (e.g. events 1-6) the event with the largest mean value is selected (typically event #1 as in B). C) Once the supra-threshold event is selected a smaller epoch is extracted that is 200 ms prior to the first supra-threshold time point (diamond in A and C) and 100 ms after this time point. D) The 300 ms window of interest is then further epoched into 20 segments that are 100 ms in duration and have 90% overlap. Each of the 20 segments is then fitted with a least squares line to obtain a slope value and residual error. Because increases in HFB response will be fit with larger positive gradients, we rank all slopes ascendingly and select the top five segments (steepest slopes), from which we identify the segment with the smallest mean squared error (best fit). The first time point of the identified segment (grey fill segment) then defines the estimated ROL for the trial of interest (blue circle in D, C & A).

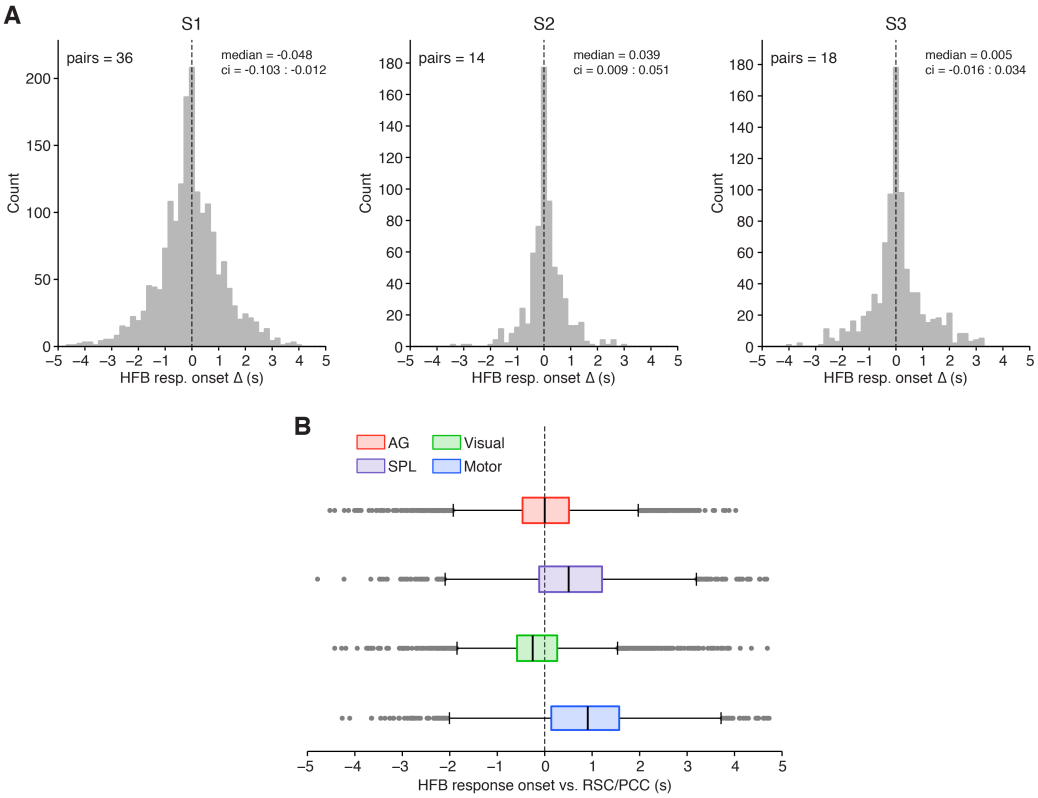

Figure S5 [Related to Figure 4]. Single subject and group distribution of HFB ROL difference comparisons

A) Histograms show the distribution of HFB ROL difference values between RSC/PCC and AG for each subject (left to right = S1-S3; pairs n = 36, 14, 18). A single observation in each plot reflects the difference in HFB ROL between a given RSC or PCC site and an AG site for a single trial of the self-episodic condition. Distribution medians are shown along with their 99% confidence interval. B) Boxplots show the full distribution of ROL difference data (all subjects) when comparing RSC/PCC onset times to AG, SPL, visual and motor sites (same data as shown in Figure 4). Boxplots display data median (black line) and interquartile range (box), with whiskers extending 1.5 times the interquartile range. Values beyond the whisker length are defined as outliers and each value is displayed as a circle with gray fill. The spread of data from these comparisons recapitulates a symmetric and zero centered distribution for RSC/PCC and AG, in contrast to the shifted distributions for active control sites.

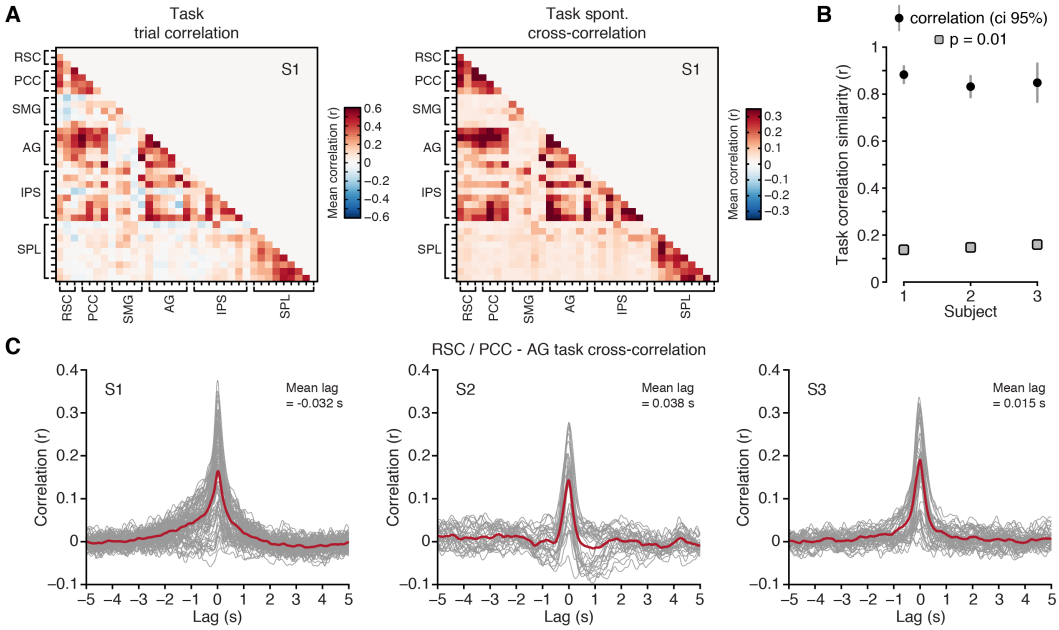

Figure S6 [Related to Figures 3 and 4]. Task cross-correlation analysis
Cross-correlation analysis of spontaneous HFB task data. A) Cross-correlation analysis revealed highly similar patterns of task connectivity (right), compared to original trial based analysis (left, S1). Cross-correlation analysis was performed on spontaneous (non-epoched) HFB task data, with correlation values reflecting the peak value across all time lags inspected (+/- 5 s) for each unique electrode pair. B) The high similarity of trial-based and spontaneous task correlation data was consistent across subjects. Plot shows similarity of task connectivity patterns for spontaneous cross-correlation and trial-based correlation data with 95% confidence intervals and p = 0.01 threshold. C) Lagged cross-correlation data is shown for all RSC/PCC – AG electrode pairs for each subject (mean distribution in red), based on spontaneous HFB task data (mean lag of maximal correlation across pairs is shown for each subject). Importantly, cross-correlation analyses closely recapitulate trial based analysis of parietal task connectivity patterns, and the close temporal coordination of RSC/PCC and AG responses during task conditions.

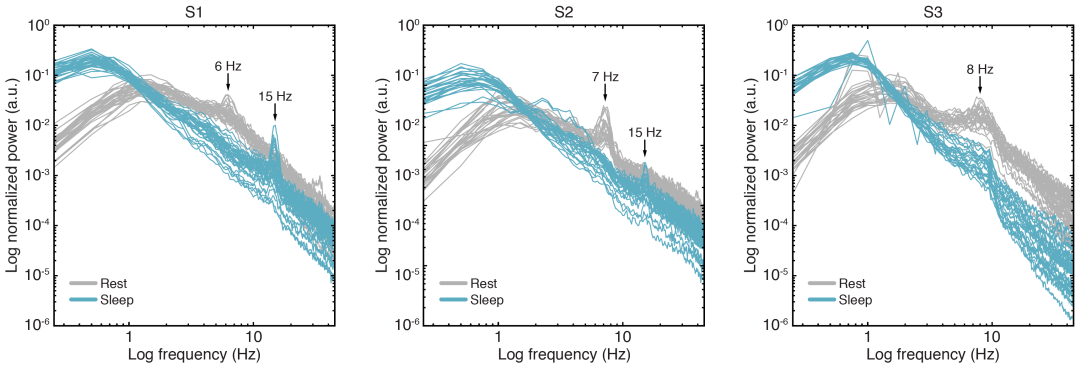

Figure S7 [Related to Figures 5 and 6]. ECoG power spectra for rest and sleep state data
Power spectra between 0.25-45 Hz are shown for rest and sleep state data for each subject. Across subjects, rest power spectra show a standard morphology for resting ECoG data, where spectral peaks are seen in the theta/alpha range as commonly observed for the parietal lobe (6, 7 and 8 Hz peaks, respectively). In contrast, sleep data show an expected shift in spectral morphology where canonical resting oscillations are attenuated and slow wave and spindle activity are greatly enhanced (spectral peaks indicative of spindle activity were most apparent in S1 and S2, both at 15 Hz). Power spectra were calculated using Welch's fast Fourier transform method with a window size of 4 seconds overlapping by 50% and shaped with a Hamming window. All data segments were truncated to be 4 minutes in duration.

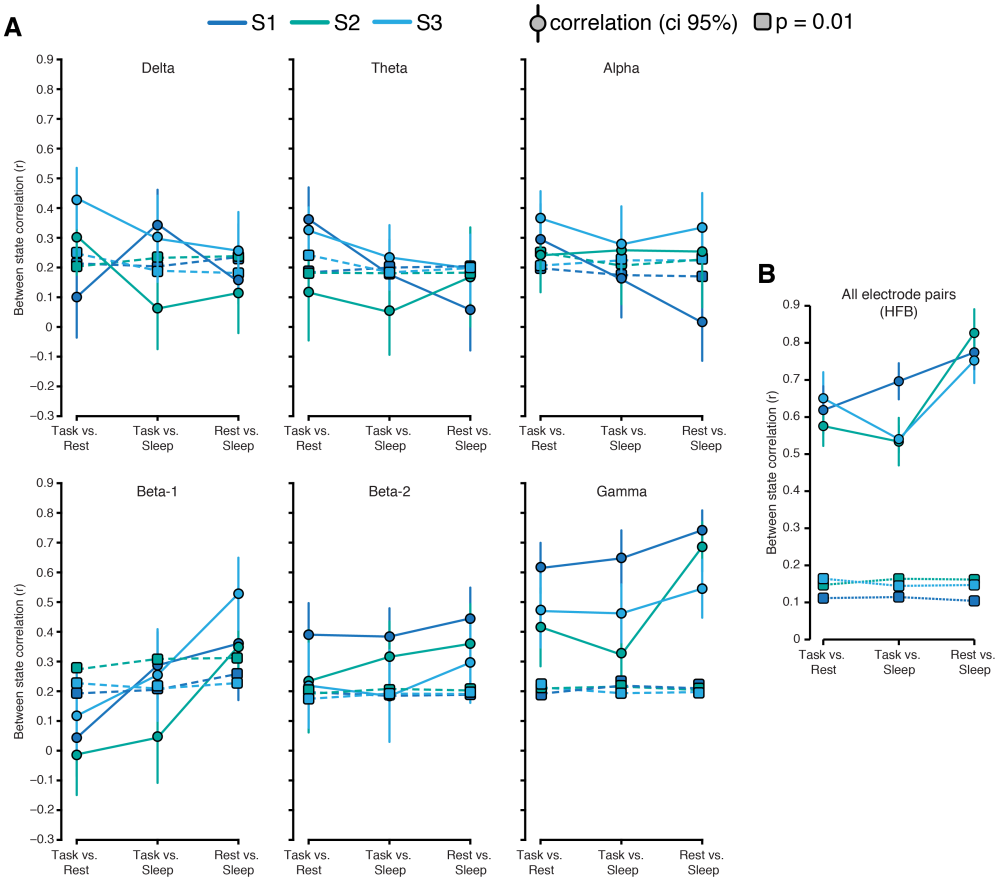

Figure S8 [Related to Figures 5 and 6]. ECoG similarity of state connectivity
A) Plots show similarity of connectivity patterns across states (task, rest & sleep) for other frequency ranges studied (Slow, < 1Hz, fluctuations of Delta, Theta, Alpha, Beta-1, Beta-2 & Gamma, as per Figure 5). Plots show similarity between states with 95% confidence intervals and p = 0.01 threshold. Only gamma band activity displays robust similarity of connectivity between states for each subject, similar to the HFB range. B) Initial analysis of HFB connectivity similarity between task, rest and sleep conditions focused only on medial-lateral parietal subregion pairs (see Figure 6E). Plot shows that including all pairs within and between parietal subregions produces highly similar and significant results across subjects (S1-S3 pairs n = 595, 351, 378). All correlation values reflect similarity of connectivity between states, with 95% confidence intervals, and p = 0.01 significance threshold.

Supplemental Tables

	Lateral Parietal				Medial Parietal			
	SPL	***IPS***	***SMG***	***AG***	***PrCC***	***PCC***	***RSC***	Total
S1	10	8	5	6	0	4	3	36
S2	6	5	0	2	7	11	0	31
S3	8	3	0	6	7	3	1	28
Total	24	16	5	14	14	18	4	95
All	59				36			

Table S1 [Related to Figure 1]. Electrode counts across parietal subregions for each subject.

Supplemental Experimental Procedures

Electrode localization

Intracranial electrodes were localized on the cortical surface using a fusion of pre- and post-operative imaging as previously described (Foster et al., 2012). In brief, post-operative CT imaging (where electrodes are clearly resolved) was aligned to a pre-operative whole brain high resolution structural T1-MRI in each subject using SPM8 (http://www.fil.ion.ucl.ac.uk/spm/). Prior to CT-MRI alignment, structural MRI data were AC-PC aligned and resampled to 1-mm isotropic voxels, also using SPM8. Electrode coordinates within each subject's headspace were then defined by the centroid of image intensity for each electrode in the aligned CT scan. Electrode coordinates were then adjusted on the cortical surface to correct for minor post-operative shifts in brain location, based on a local projection performed separately for each strip and grid (Hermes et al., 2010). Cortical surface reconstructions were obtained for each subject based on manual white matter segmentation performed using ITKGray (http://vistalab.stanford.edu/newlm/index.php/ItkGray). The cortical location of electrodes was subsequently confirmed by direct comparison with intra-operative photography (during implantation and explantation) and with electrical brain stimulation data. For group data plots, each subject's electrode coordinates were realigned to a normalized brain (MNI Colin 27; http://www.bic.mni.mcgill.ca/ServicesAtlases/Colin27), following the same procedure. As normalization of electrode locations for group plotting produces heterogeneous sampling across cortex, all group cortical surface plots (e.g., Figure 6) are corrected relative to electrode density. This density correction is estimated by applying a unit value to all electrodes to obtain a weighting value, which is subtracted when plotting real data.

Electrode anatomical classification

Once the cortical location of electrodes was obtained for each subject, we identified all electrodes falling within the medial and lateral parietal cortex and classified them into parietal subregions (using surface projections and 3D images). We note that our focus within the parietal cortex excludes the post-central gyrus medially and laterally, and is therefore best referred to as posterior parietal cortex. All electrode classifications were performed with reference to individual subject neuroanatomy.

For the lateral parietal cortex (LPC), we defined four subregions: i) superior parietal lobule (SPL, BA 7), which reflects dorsal parietal cortex medial to the intraparietal sulcus (IPS), and extending posterior from the post-central sulcus to BA 19. ii) IPS, which runs longitudinally through LPC from approximately the transverse occipital sulcus (TOS) towards the post-central sulcus. iii) supramarginal gyrus (SMG, BA 40), located in the inferior parietal lobule (IPL), ventral to the IPS and superior to, or surrounding, the termination the lateral fissure. iv) angular gyrus (AG, BA 39), also located in the IPL, posterior to the SMG and surrounding the termination of the superior temporal sulcus (STS). In summary, the lateral parietal subregions of interest were SPL, IPS, SMG and AG.

For the medial parietal cortex (MPC), we also focused on regions posterior to the post-central sulcus (medial posterior parietal cortex), which is best defined by the medial cortex posterior to the marginal branch of the cingulate sulcus (mbCGS) and anterior/dorsal to the parieto-occipital sulcus (POS). Our previous anatomical work

has referred to this region as the posteromedial cortex (Parvizi et al., 2006). Within the MPC, we defined 3 subregions: i) precuneus cortex (PrCC, BA 7m), which is bounded anteriorly by the mbCGS, posteriorly by the POS and inferiorly by BA 31 and BA 23. ii) posterior cingulate cortex (PCC, BA 23), which lies inferior to the PrCC and extends anteriorly along the cingulate gyrus to mid cingulate cortex (MCC, BA 24) and ventrally to the POS. iii) retrosplenial cortex (RSC, BA 29/30), which lies caudal to the PCC and extends ventrally from the POS to dorsal PCC, predominantly occupying the callosal sulcus. Importantly, we note that identifying medially exposed gyral cortex as RSC, as distinct from ventral PCC, is debated and the use of RSC here is best viewed as a locational, not cytoarchitectural, descriptor (Vogt et al., 1995; Vogt et al., 2001). Given this difficulty, we perform several analyses with PCC and RSC electrodes collapsed together as one anatomical region. In summary, the medial parietal subregions of interest were PrCC, PCC and RSC. See Figure 1A for anatomical divisions and Table S1 for counts of electrodes across subregions.

Experimental task - ECoG

Historically, the DMN was first identified because of its consistent deactivation during many cognitive tasks that required directed attention, and working memory (Raichle et al., 2001). Subsequent neuroimaging work has reported DMN activation during a collection of tasks that include episodic/autobiographical retrieval or tasks that require self-referential cognition, moral judgment, theory of mind and semantic processing (Andrews-Hanna et al., 2014; Binder and Desai, 2011; Buckner et al., 2008; Mullally and Maguire, 2013; Renoult et al., 2012; Spreng et al., 2009). With this literature in mind, our experimental task sought to probe these different domains associated with DMN activity (both activation and deactivation), within a single experiment that required minimal participant training and allowed comparable stimuli and decision/response outputs across conditions.

Four of the five response conditions were sentences describing episodic and/or personal attributes; these were: 1) self-episodic (e.g., "*I ate candy yesterday*"); 2) self-semantic (e.g., "*I eat a lot of candy*"); 3) self-judgment (e.g., "*I am honest*"); 4) other-judgment (e.g., "*My neighbor is honest*") (see Figure 1). For the other-judgment condition, subjects were informed prior to the task to select a single neighbor (current or past) and to consistently answer with respect to that individual only. The fifth response condition contained completed arithmetic equations (5) math, e.g., "9 + 86 = 95"). All equations were additions of a single-digit and double-digit number (matched for equation position), and limited to double-digit answers (50% correct/incorrect). Randomly interleaved between stimuli was a fixation condition, (6) rest, where a central fixation crosshair was presented on the screen for 5 or 10 s. For all response conditions (1-5), subjects provided a true or false response via a handheld keypad using either the '1' (true) or '2' (false) key (using their right hand, contralateral to the implantation hemisphere). Subjects were instructed to perform the task as accurately and as quickly as possible. During each experimental run, stimuli were presented in a random order and were self-paced, advancing to the next trial after the subjects' response. If subjects did not respond within 15 s the task automatically advanced to the next trial. The inter-stimulus interval (ISI) was 200 ms for all trials other than for the rest condition, where there was no ISI after the trial (i.e., no ISI for any trials following a rest trial).

All stimuli were presented in white font on a black background using Psychtoolbox (http://psychtoolbox.org/HomePage) in MATLAB (MathWorks). To

increase trial number and maintain subject performance, the experiment was broken into two separate runs (Task-1 & Task-2). Each experimental run on average lasted 12.50 ± 1.64 minutes. Subjects were allowed a short break in between the experimental runs. Each task run contained different stimuli for all conditions. For each run, there were 25 trials of the sentence conditions (Conditions 1-4) and 40 trials of the math condition (Condition 5). The randomization of the interleaved rest condition (6) resulted in an average of 36 trials per task run. All behavioral data was logged locally on the task presentation laptop, with trial events being logged and temporally synchronized with the ECoG recording via a photodiode trigger.

While the four sentence conditions are hypothesized to differentially activate DMN regions, the math condition serves to engage the putative antagonistic functions of this network, whereby states of goal-directed attention and working memory often suppress activity in DMN subregions. Our previous work has confirmed this prediction electrophysiologically in the medial parietal cortex (Foster et al., 2012). Importantly, all conditions are similar in requiring each stimulus to be read and require a true/false judgment and corresponding motor response.

As noted above, the DMN displays selective task deactivation during conditions that require goal-directed attention and working memory. We and other investigators have shown that basic arithmetic processing (e.g. simple addition) effectively captures this kind of cognitive demand and robustly deactivates DMN regions (Foster et al., 2012; Kennedy and Courchesne, 2008). Importantly in our task, the math condition we employed allowed us to selectively deactivate putative DMN regions with visual stimuli that are presented as readable text and require a basic true/false button press response – matching other task conditions. Furthermore, a wealth of work from human brain imaging, and also electrophysiology from our own group, has shown that lateral parietal regions close to, but outside of, the DMN are strongly activated during numerical processing (e.g., anterior IPS, (Dastjerdi et al., 2011; Nieder and Dehaene, 2009)). Therefore, the math condition in our experiment serves an important control function for confidently identifying DMN parietal regions and dissociating them from nearby regions that are involved in non-DMN functions such as numerical processing.

Regarding the other active task conditions, the self-episodic ("I drank coffee this morning"), the self-semantic ("I drink coffee often") and the self-judgment ("I'm a kind person") conditions all require some level of self-referential processing, however they differ in their degree of episodic specificity. Also, all of these conditions, including the 'other-judgment' condition ("My neighbor is a kind person"), require the retrieval of basic semantic and conceptual knowledge. Therefore, specific response profiles across these conditions, within DMN regions, may favor different contemporary accounts of DMN function that emphasize episodic (Rugg and Vilberg, 2013), self-referential (Buckner and Carroll, 2007) or semantic processing (Binder and Desai, 2011).

HFB response latency

In order to characterize the latency of activation across electrodes for the self-episodic condition, we estimated the HFB response onset latency (ROL), using a modified version of a previously described technique (Foster et al., 2012). HFB ROL was estimated using the following steps: i) for each electrode, the entire normalized HFB amplitude time series (calculated above) was smoothed by convolution with a 50

point (~115 ms) Gaussian window; ii) a null distribution of epoched responses was then generated by creating 1000 mean HFB responses based on a random sampling of all experimental trials (epoch duration = max epoch duration across all conditions; trials# = mean number of trials across all conditions). Based on this distribution a response threshold was then defined for all epoch time points as two positive standard deviations from the mean; iii) for each condition of interest, the smoothed HFB time series was then epoched (including the pre-stimulus period) for trial-wise onset estimation; iv) for a given trial, supra threshold response(s) in HFB amplitude were identified by logging time points where the HFB amplitude was above threshold (defined in ii) for successive data points (>100 ms). When multiple (discontinuous) responses were identified for an epoch, the response with the largest mean value was selected. An onset window of interest was then defined as 200 ms before and 100 ms after the first supra threshold time point of the identified HFB amplitude response (Note: if no supra threshold response was identified, onset estimation was not performed for that trial); v) HFB data within this 300 ms onset window of interest was then broken into 100 ms bins with 90% overlap (20 bins in total), each fitted with a least squares line to estimate slope and residual error; vi) fitted slopes from all of the bins were then ranked ascendingly and the bin with the smallest mean-square error from the top five ranked slopes was selected. The first time point of the selected bin defined the HFB amplitude response onset latency for each trial. This procedure was performed for each channel for the self-episodic condition only. Finally, we note that as outliers can only be positive for latency data (biasing distributions to a positive skew), we use the median latency value whenever trials are collapsed.

Connectivity analyses – ECoG & fMRI

Connectivity analyses focused on correlated HFB (ECoG) and BOLD (fMRI) activity. For all data, correlation values were estimated via Pearson's correlation coefficient (r) between all sites (electrodes or ROIs), producing a correlation matrix for each data set. Correlation p-values were estimated using a conservative block swap permutation test (1000 iterations) as previously described (Canolty et al., 2006; Foster and Parvizi, 2012) and corrected within subjects for multiple comparisons (i.e., for all unique electrode pairs constituting the correlation matrix) using the false discovery rate (FDR) with a threshold (q) of 0.01 (Benjamini et al., 2001). We note that permutation based p-value estimation was calculated with a bias correction such that the lowest achievable p-value was 1/1000+1. This correction avoids the occurrence of p-values equal to zero (for 1000 iterations), and limits the calculation time (i.e., additional iterations) required for estimating the non-zero value of small p-values < 0.001.

For Figure 7B, we selected a PCC ROI in S3 and performed a voxel wise whole-brain functional connectivity analysis for this seed: the seed ROI mean time series was compared with the time series of individual voxels using a Pearson correlation. Clusters in the resulting whole-brain functional connectivity map have a threshold for height ($p < 0.001$) and extent ($p < 0.001$, uncorrected). A template-matching analysis based on Greicius et al. (2004) identified the functional connectivity map as the default network ($r = 0.36$, $p < 0.001$).

Statistical analyses

For statistical testing, parametric methods were used for normal data. For non-normal or small sample size data resampling methods were employed, using 1000 sample

iterations. For point estimates of mean or median, confidence intervals are reported based on resampling estimation (1000 sample iterations). For correlational analyses between channels, multiple comparisons were controlled using false discovery rate (FDR, q = 0.01). To compare correlation matrices between states, we performed Mantel's test of matrix similarity using 1000 permutations. To satisfy normality, correlation matrices were adjusted using a Fisher *r-z* transform prior to performing statistical testing. All permutation testing is performed as a two-sided comparison.

Supplemental References

Andrews-Hanna, J.R., Smallwood, J., and Spreng, R.N. (2014). The default network and self-generated thought: component processes, dynamic control, and clinical relevance. Ann N Y Acad Sci 1316, 29-52.

Benjamini, Y., Drai, D., Elmer, G., Kafkafi, N., and Golani, I. (2001). Controlling the false discovery rate in behavior genetics research. Behav Brain Res 125, 279-284.

Binder, J.R., and Desai, R.H. (2011). The neurobiology of semantic memory. Trends Cogn Sci 15, 527-536.

Buckner, R.L., Andrews-Hanna, J.R., and Schacter, D.L. (2008). The brain's default network: anatomy, function, and relevance to disease. Ann N Y Acad Sci 1124, 1-38.

Buckner, R.L., and Carroll, D.C. (2007). Self-projection and the brain. Trends Cogn Sci 11, 49-57.

Canolty, R.T., Edwards, E., Dalal, S.S., Soltani, M., Nagarajan, S.S., Kirsch, H.E., Berger, M.S., Barbaro, N.M., and Knight, R.T. (2006). High gamma power is phase-locked to theta oscillations in human neocortex. Science 313, 1626-1628.

Dastjerdi, M., Foster, B.L., Nasrullah, S., Rauschecker, A.M., Dougherty, R.F., Townsend, J.D., Chang, C., Greicius, M.D., Menon, V., Kennedy, D.P., and Parvizi, J. (2011). Differential electrophysiological response during rest, self-referential, and non-self-referential tasks in human posteromedial cortex. Proc Natl Acad Sci U S A 108, 3023-3028.

Foster, B.L., Dastjerdi, M., and Parvizi, J. (2012). Neural populations in human posteromedial cortex display opposing responses during memory and numerical processing. Proc Natl Acad Sci U S A 109, 15514-15519.

Foster, B.L., and Parvizi, J. (2012). Resting oscillations and cross-frequency coupling in the human posteromedial cortex. Neuroimage 60, 384-391.

Greicius, M.D., Srivastava, G., Reiss, A.L., and Menon, V. (2004). Default-mode network activity distinguishes Alzheimer's disease from healthy aging: evidence from functional MRI. Proc Natl Acad Sci U S A 101, 4637-4642.

Hermes, D., Miller, K.J., Noordmans, H.J., Vansteensel, M.J., and Ramsey, N.F. (2010). Automated electrocorticographic electrode localization on individually rendered brain surfaces. J Neurosci Methods 185, 293-298.

Kennedy, D.P., and Courchesne, E. (2008). Functional abnormalities of the default network during self- and other-reflection in autism. Soc Cogn Affect Neurosci 3, 177-190.

Mullally, S.L., and Maguire, E.A. (2013). Memory, Imagination, and Predicting the Future: A Common Brain Mechanism? Neuroscientist 20, 220-234.

Nieder, A., and Dehaene, S. (2009). Representation of number in the brain. Annu Rev Neurosci 32, 185-208.

Parvizi, J., Van Hoesen, G.W., Buckwalter, J., and Damasio, A. (2006). Neural connections of the posteromedial cortex in the macaque. Proc Natl Acad Sci U S A 103, 1563-1568.

Raichle, M.E., MacLeod, A.M., Snyder, A.Z., Powers, W.J., Gusnard, D.A., and Shulman, G.L. (2001). A default mode of brain function. Proc Natl Acad Sci U S A 98, 676-682.

Renoult, L., Davidson, P.S., Palombo, D.J., Moscovitch, M., and Levine, B. (2012). Personal semantics: at the crossroads of semantic and episodic memory. Trends Cogn Sci 16, 550-558.

Rugg, M.D., and Vilberg, K.L. (2013). Brain networks underlying episodic memory retrieval. Curr Opin Neurobiol 23, 255-260.

Spreng, R.N., Mar, R.A., and Kim, A.S. (2009). The common neural basis of autobiographical memory, prospection, navigation, theory of mind, and the default mode: a quantitative meta-analysis. J Cogn Neurosci 21, 489-510.

Vogt, B.A., Nimchinsky, E.A., Vogt, L.J., and Hof, P.R. (1995). Human cingulate cortex: surface features, flat maps, and cytoarchitecture. J Comp Neurol 359, 490-506.

Vogt, B.A., Vogt, L.J., Perl, D.P., and Hof, P.R. (2001). Cytology of human caudomedial cingulate, retrosplenial, and caudal parahippocampal cortices. J Comp Neurol 438, 353-376.